Time-resolved interplay between superradiant and subradiant states in superradiance lattices of Bose-Einstein condensates

Chengdong Mi,[1,2] Khan Sadiq Nawaz,[1,2] Liangchao Chen,[1,2,*] Pengjun Wang,[1,2] Han Cai,[3,†] Da-Wei Wang,[3,4] Shi-Yao Zhu,[3] and Jing Zhang[1,2,‡]

[1]*State Key Laboratory of Quantum Optics and Quantum Optics Devices, Institute of Opto-Electronics, Shanxi University, Taiyuan 030006, China*

[2]*Collaborative Innovation Center of Extreme Optics, Shanxi University, Taiyuan 030006, China*

[3]*Interdisciplinary Center for Quantum Information, State Key Laboratory of Modern Optical Instrumentation, and Zhejiang Province Key Laboratory of Quantum Technology and Device, Department of Physics, Zhejiang University, Hangzhou 310027, Zhejiang Province, China*

[4]*CAS Center for Excellence in Topological Quantum Computation, University of Chinese Academy of Sciences, Beijing 100190, China*

(Received 28 May 2021; accepted 12 October 2021; published 28 October 2021)

The collective spontaneous emission of many atoms is significantly different from that of a single atom, depending on the geometry and the phase correlation of atomic ensembles. However, experimental observation of arbitrary superradiant and subradiant states of atoms remains challenging due to the difficulties in both preparation and detection of those states. Here we report the time-resolved observation of superradiance from a timed Dicke state in a momentum-space superradiance lattice of Bose-Einstein condensates, which enables an *in situ* measurement of the coherent lattice dynamics involving both superradiant and subradiant states. The long-lasting oscillation in the superradiant emission is contributed by population transport from the subradiant states in the superradiance lattice. This work paves the way to prepare and observe subradiant states, which has promising applications in quantum information processing.

DOI: 10.1103/PhysRevA.104.043326

I. INTRODUCTION

Superradiance [1,2] is an important phenomenon of collective light-matter interaction. The decay rate of an atomic ensemble with a proper phase correlation can be significantly enhanced by the cooperativity between atoms. Such atomic coherence can be spontaneously generated either by inverting the population of the atoms [3,4] or by collectively exciting the atoms with a weak light field [5–10]. In the latter case, the coherence is transferred from light to atom by the collective absorption of a single photon in an extended ensemble of atoms, such that the atoms are prepared in a timed-Dicke state (TDS) [5,6] (also known as the spin-wave state [11]) $|\boldsymbol{k}\rangle = 1/\sqrt{N}\sum_j \exp(i\boldsymbol{k}\cdot\boldsymbol{r}_j)|g_1, g_2, \ldots, e_j, \ldots, g_j\rangle$, where $\boldsymbol{r}_j$ is the position of the jth atom with ground state g_j and excited state e_j. The term "timed" indicates the phase correlation factor $\exp(i\boldsymbol{k}\cdot\boldsymbol{r})$ which carries the excitation time of the atom at position $\boldsymbol{r}$ [5].

The most straightforward approach to investigate the decay dynamics of a TDS is to measure the cooperative emission right after the excitation. The superradiant TDS with $|\boldsymbol{k}| = \omega/c$, with ω being the atomic transition frequency and c being the speed of light, is featured by a directional emission along $\boldsymbol{k}$ with a superradiant decay rate proportional to the number of atoms. These states can be directly prepared and have been extensively investigated in atomic ensembles [12–17]. However, the complete description of the cooperative emission will include those TDSs with quasimomenta $|\boldsymbol{k}| \neq \omega/c$. These states are called subradiant TDSs with smaller decay rates compared to that of a single atom [18]. Temporal observation of subradiant TDSs [19,20] is difficult because those states cannot be prepared directly or detected efficiently since their radiation direction is random. In a recent work [20,21], ultrafast switching between a pair of superradiant and subradiant TDSs was realized by successively applying two counterpropagating coupling fields to steer phase correlation [22].

Here we report the time-resolved observation of superradiance from a one-dimensional bipartite superradiance lattice (SL) [19,23]. The coherent transport of excitations along the lattice depends on the band structure and the site-dependent cooperative decay rates, for superradiant and subradiant decay. After exciting the atomic ensemble with a nanosecond excitation pulse, we collect the directional emission to measure the population of the corresponding superradiant TDS. The typical signal contains two temporally separable parts: (1) the enhanced exponential decay immediately after the excitation and (2) the oscillating decay due to the population transport from the subradiant states. The first part demonstrates the enhanced collective decay of the superradiant TDS,

*Corresponding author: chenlchao87@sxu.edu.cn
†hancai@zju.edu.cn
‡jzhang74@sxu.edu.cn, jzhang74@yahoo.com

and the latter part manifests the energy-band structure, as well as the cooperative dissipation of the subradiant TDSs in the coherent lattice dynamics.

II. EXPERIMENTAL SCHEME

In our experiment, we prepare a pure Bose-Einstein condensate (BEC) with typically 5×10^5 ^{87}Rb atoms in the $|g\rangle \equiv |F = 2, m_F = 2\rangle$ hyperfine ground state confined in a cross-beam dipole trap at a wavelength near 1064 nm. The geometric mean of trapping frequencies is $\overline{\omega} \simeq 2\pi \times 80$ Hz. The atomic size is estimated in the Thomas-Fermi regime to be 20 μm according to the scattering length for the $|g\rangle$ state at zero magnetic field with about $100a_0$, corresponding to an optical thickness $b \approx 80$ for the excitation beam with zero detuning. A homogeneous bias magnetic field along the z axis (gravity direction) is provided with $B_0 = 2$ G by a pair of coils operating in the Helmholtz configuration. We choose the D_1 line (around 795 nm) of the ^{87}Rb atom with a simple three-level Λ-type model. The D_1 transition between $|g\rangle$ and an atomic excited state $|e\rangle \equiv |F' = 1, m_{F'} = 1\rangle$ is pumped by a weak excitation laser pulse with wave vector $\boldsymbol{k}_f$, whose 4-ns pulse width is much shorter than the single-atom lifetime $1/\gamma = 27$ ns. Two coupling beams with wave vectors $\boldsymbol{k}_1$ and $\boldsymbol{k}_2$ are continuously applied to couple $|e\rangle$ to a hyperfine ground state $|m\rangle \equiv |F = 1, m_F = 1\rangle$.

The experimental setup, atomic configuration, and time sequence of the coupling and excitation lasers are shown in Fig. 1. After the preparation of BEC in the crossed-beam dipole trap, the two coupling beams are turned on (using an acousto-optic modulator as a switch) for 380 μs to form an interference pattern at the position of the BEC. During this time, 1000 shots of 4-ns excitation pulses are sent to the atoms, controlled by the electro-optical modulator for amplitude modulation (EOM-AM; EOSPACE, fiber-coupled broadband 10–40+ GHz, low-loss $LiNbO_3$ modulator model AZ-0S5-20-PFU-780-UL). The EOM-AM is controlled through an arbitrary function generator by a 3-MHz pulse signal which also triggers the single-photon counting module for synchronization. The coupling laser beams have a waist ($1/e^2$ radius) of about 280 μm at the BEC position. The weak excitation light used to pump the atoms from $|g\rangle$ to $|e\rangle$ has a waist of about 600 μm. The frequencies of the coupling and excitation laser are locked, which was described in our previous work [19]. After 1000 shots of the excitation laser, 24% of the atoms are left in the cloud near the critical temperature of the BEC. This is one run of the experiment, after which we prepare a new sample of the BEC in 45 s. The photon number is around 0.083 per shot as counted by the single-photon detector. Each time-resolved decay curve of the scattering light in this work is obtained by a total of 300 runs of such sequences.

A photon detector with a solid angle ~0.02 sr is used to collect the emission along the backward direction $\boldsymbol{k}_b = \boldsymbol{k}_f - \boldsymbol{k}_1 + \boldsymbol{k}_2$. Owing to the small solid angle, we can neglect the contributions from other TDSs with $\boldsymbol{k} \neq \boldsymbol{k}_b$ [24]. Hence, the emission is approximately proportional to the probability of TDSs with a quasimomentum $\boldsymbol{k}_b$ [20],

$$I(t) \propto \langle \hat{a}^\dagger_{\boldsymbol{k}_b} \hat{a}_{\boldsymbol{k}_b} \rangle, \tag{1}$$

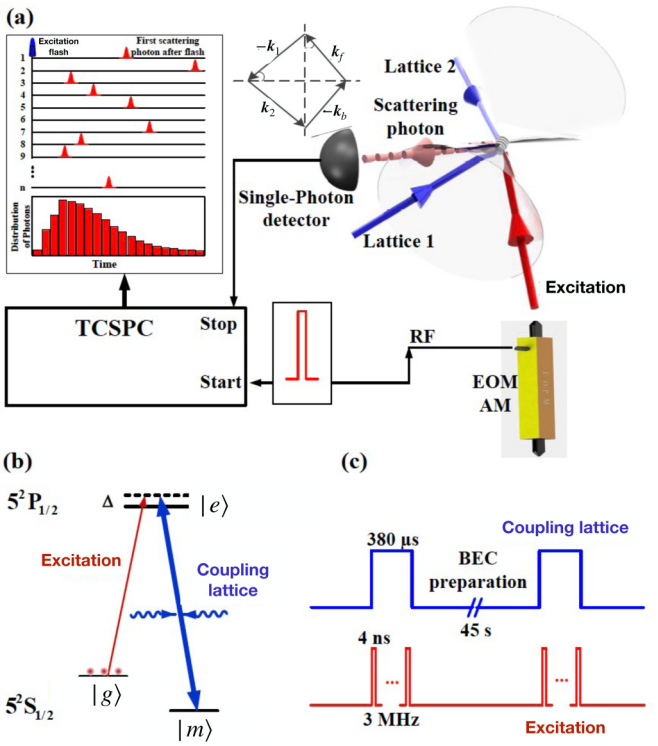

FIG. 1. Experimental setup and the atomic levels. (a) The experimental setup. A pair of strong coupling laser beams (lattice 1 and lattice 2) drives the transition between $|m\rangle \equiv |F = 1, m_F = 1\rangle$ and $|e\rangle \equiv |F' = 1, m_{F'} = 1\rangle$ and forms a superradiance lattice. The excitation light illuminates the BEC, and the scattering light is detected by the single-photon detector and recorded by the TCSPC method. The inset panel shows the schematic TCSPC wave-form generation. The inset wave-vector configuration of $\boldsymbol{k}_i$ shows the phase matching between the excitation, coupling, and scattered lights. (b) The energy-level scheme of the $5^2S_{1/2}$-$5^2P_{1/2}$ D_1 line transition of ^{87}Rb. The weak excitation light drives the transition between the ground state $|g\rangle \equiv |F = 2, m_F = 2\rangle$ and the excited state $|e\rangle$. Atoms are initially prepared in the ground state $|g\rangle$. (c) Schematic timing of the light-pulse sequences, with blue (dark gray) for the coupling lights and red (light gray) for the excitation light. EOM-AM: Electro-optical amplitude modulator; TCSPC: Time-correlated single-photon counting.

where $\hat{a}^\dagger_{\boldsymbol{k}} = 1/\sqrt{N} \sum_j e^{i\boldsymbol{k}\cdot\boldsymbol{r}_j} |e_j\rangle\langle g_j|$ is the TDS creation operators for the $|e\rangle$ state and $\langle\cdot\rangle$ is the expectation value. The temporal profile of the collected emission is resolved by the time-correlated single-photon counting (TCSPC) method with a time bin of 64 ps, which enables a subnanoscale resolution in the time domain. The inset in Fig. 1(a) schematically shows the distribution of the detected photons as a function of time. Typical signals are shown in Figs. 2 and 3, which contain a fast exponential decay and a subsequent oscillation.

III. MODEL AND RESULTS

The exponential decay curve shaded yellow in Fig. 2(b) represents the superradiant decay of the TDS with $|\boldsymbol{k}_b\rangle$ prepared by the excitation pulse. The Hamiltonian involving the

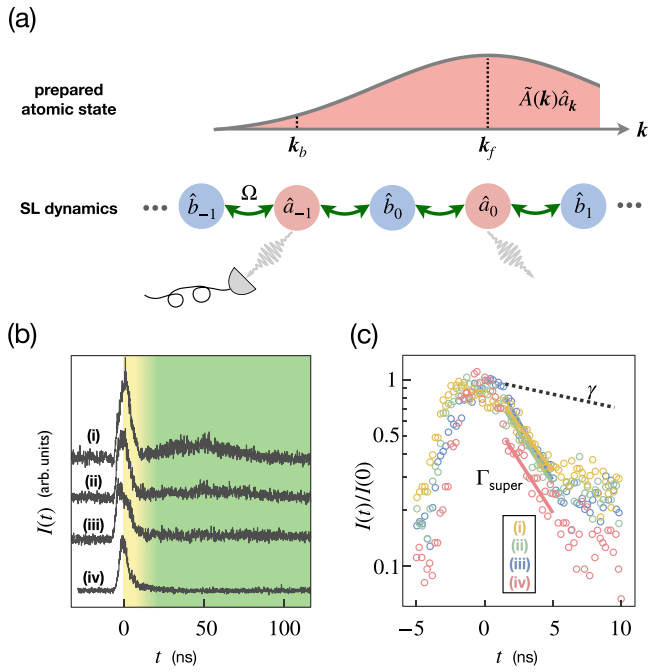

FIG. 2. Atomic state preparation and the time-resolved decay of the scattered light. (a) The spatially attenuated excitation field creates a superposition of superradiant TDSs with a momentum-space distribution centered around $\boldsymbol{k}_f$. (b) The power of each coupling field is (i) and (iv) 30, (ii) 20, and (iii) 10 μW, and the frequency detuning with atomic transition is (i)–(iii) 0 and (iv) 400 MHz. (c) The time-dependent superradiant signal is plotted in logarithmic scale and linearly fitted to obtain the superradiant decay rate $\Gamma_{\text{super}} = (7.03 \pm 0.33)\gamma$. Throughout the experiment, we keep the power of the excitation field at 3 μW and its frequency resonant with the atomic transition between $|g\rangle$ and $|e\rangle$.

excitation field is

$$V = \sum_j A(\boldsymbol{r}_j) e^{i\boldsymbol{k}_f \cdot \boldsymbol{r}_j} |e_j\rangle\langle g_j| + \text{H.c.}$$
$$= \int d\boldsymbol{k} \tilde{A}(\boldsymbol{k}) \hat{a}_{\boldsymbol{k}}^\dagger + \text{H.c.}, \quad (2)$$

where the excitation pulse collectively prepares a single-excitation state with a local amplitude $A(\boldsymbol{r}_j)$ and a local phase factor $\exp(i\boldsymbol{k}_f \cdot \boldsymbol{r}_j)$ for the jth atom. Meanwhile, $\tilde{A}(\boldsymbol{k})$ is the corresponding momentum-space distribution of the prepared excitation in the basis of the TDS. In previous studies [12–17], the optical depth was usually kept low to ensure the amplitude profile of the excitation field was nearly uniform across the atomic ensemble $A(\boldsymbol{r}) = \Omega_0$, where Ω_0 is the Rabi frequency of the excitation field. In that case the excitation pulse excites only a single TDS with $\boldsymbol{k}_f$, i.e., $\tilde{A}(\boldsymbol{k}) \approx \sqrt{N}\Omega_0 \delta(\boldsymbol{k} - \boldsymbol{k}_f)$. Here we use a resonant field to pump a dense atomic medium in the experiment. The excitation field, whose amplitude is attenuated exponentially along the propagation, prepares a superposition of TDSs with momentum-space distribution around $\boldsymbol{k}_f$, as schematically shown in Fig. 2(a). Along the propagation direction, the power of the excitation laser is exponentially attenuated $A(\boldsymbol{r}) = \Omega_p \exp(-\eta \boldsymbol{k}_f \cdot \boldsymbol{r})$ with the attenuation factor η, and the momentum-space distribution is $\tilde{A}(\boldsymbol{k}) \propto 1/[\eta - i(\boldsymbol{k} - \boldsymbol{k}_f) \cdot \boldsymbol{n}_{||}/|\boldsymbol{k}_f|]$, where $\boldsymbol{n}_{||}$ is the unit vector along the propagation direction. One remark is that a thick optical depth is not a requirement to observe the band dynamics, as discussed below, but excites the $|\boldsymbol{k}_b\rangle$ TDS so that we are able to observe exponential decay in the backward direction immediately after the excitation pulses.

In Fig. 2(c), we plot the signal in logarithmic scale to highlight the exponential decay. By linearly fitting the signal between 2 and 5 ns, we obtain the superradiant decay rate $\Gamma_{\text{super}} = (7.03 \pm 0.33)\gamma$. Γ_{super} is the same for different configurations of the coupling fields. Following the superradiant signal, the slow oscillation shaded green in Fig. 2(b) is determined by the coherent dynamics of the excitation in a bipartite one-dimensional lattice [19,23,25]. The formation of the momentum-space lattice can be understood by considering the phase switching between TDSs. Either lattice beam can drive the atomic transition from the atomic internal state $|e\rangle$ to $|m\rangle$, simultaneously assigning a local phase factor $e^{-i\boldsymbol{k}_{1(2)}\cdot\boldsymbol{r}}$ in the transition. The lattice beams provide a "hopping" of the excitation between the site with momentum $\boldsymbol{k}$ and two neighbouring sites with momentum $\boldsymbol{k} - \boldsymbol{k}_1$ and $\boldsymbol{k} - \boldsymbol{k}_2$. The Hamiltonian of the SL reads $H = \sum_l \Delta \hat{b}_l^\dagger \hat{b}_l + \Omega(\hat{a}_l^\dagger \hat{b}_l + \hat{a}_l^\dagger \hat{b}_{l+1} + \text{H.c.})$, where $\hat{b}_{\boldsymbol{k}}^\dagger = 1/\sqrt{N}\sum_j e^{i\boldsymbol{k}\cdot\boldsymbol{r}_j}|m_j\rangle\langle g_j|$ is the TDS creation operator for the $|m\rangle$ state. For notational convenience, we denote $\hat{a}_l \equiv \hat{a}_{\boldsymbol{k}_f + l(\boldsymbol{k}_1 - \boldsymbol{k}_2)}$ and $\hat{b}_l \equiv \hat{b}_{\boldsymbol{k}_f - \boldsymbol{k}_1 + l(\boldsymbol{k}_1 - \boldsymbol{k}_2)}$. $\Delta = \nu - \omega_{em}$ is the frequency detuning between the coupling fields and the atomic transition, and Ω is the Rabi frequency.

The signal of the SL dynamics can be separated from the fast decay signal in the time domain. The timescale of the SL dynamics is determined by the band structure, i.e., the power and frequency of the coupling fields Ω and Δ. In Fig. 2(b), lines (i)–(iii) show the SL dynamics for different energy powers of the resonant coupling laser with 30, 20, and 10 μW, which correspond to $\Omega = 4.0$, 3.3, and 2.3 MHz $\ll \Gamma_{\text{super}}$, respectively. The signal decreases when the coupling strength in the SL decreases since the excitation decays while being transferred to the site of $|\boldsymbol{k}_b\rangle$. For comparison, we also tune the frequency of the lattice beam away from resonance between $|e\rangle \to |m\rangle$ with a detuning $\Delta = 400$ MHz and keep $\Omega = 4$ MHz in line (iv) in Fig. 2(b). The green-shaded signal is completely suppressed. It can be used to exclude the grating effect induced by the atomic density modulation [26] since the potential depth for the $|g\rangle$ level $\Omega^2/(6.8\text{GHz} + \Delta)$ changes less than 5% from $\Delta = 0$ to 400 MHz, which cannot account for the complete disappearance of the oscillation. However, a 400-MHz on-site energy difference between two sublattices of the SL is large enough to inhibit lattice transport with a hopping strength $\Omega \ll \Delta$.

The oscillation in the superradiance signal results from the quantum beating between the two energy bands of the SL. In Fig. 3, we present the SL dynamics with different detunings Δ and keep $\Omega = 4$ MHz. The energy difference between the two bands determines the oscillation period, which is similar to the Autler-Townes splitting [27,28]. For $\Delta = 0$, two energy bands of the SL touch, and the wide bandwidth leads to a quickly collapsing oscillation, which corresponds to a single peak for $\Delta = 0$ in Fig. 3(g) and a strongly damped oscillation for $\Delta = \pm 10$ MHz in Figs. 3(e) and 3(f). On the contrary, we notice a single frequency oscillation owing to a

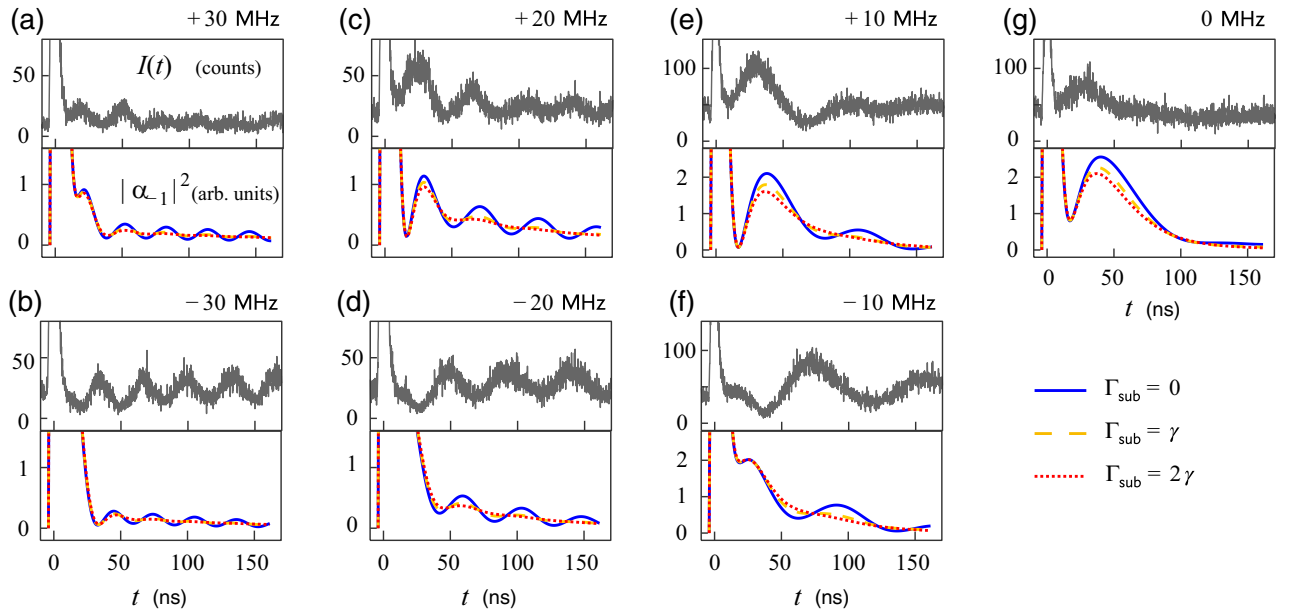

FIG. 3. Time-resolved decay of the scattering light for different detunings of the coupling laser. The coupling laser is detuned from the $|e\rangle$ to $|m\rangle$ transition by (a) 30, (b) −30, (c) 20, (d) −20, (e) 10, (f) −10, and (g) 0 MHz. The power of each coupling field is 10 μW. In the simulation, $\Gamma_{\text{super}} = 7\gamma$ and $\Omega = 4$ MHz are taken according to the experimental parameters. The attenuation factor $\eta = 0.5$ is the only free parameter in the fitting. The numerical computing results with $\Gamma_{\text{sub}} = 0$ (blue solid), γ (yellow dashed), and 2γ (red dotted), are plotted for comparison.

bandwidth much smaller than the band gap when $\Delta \gg \Omega$ in Figs. 3(a)–3(d).

We also notice that the coherent band oscillation for opposite detunings exhibits an approximately π-phase difference, as shown in Fig. 4(a). We attribute this shift to the interference between different TDSs. It can be reproduced in the numerical simulation by considering the excitation field attenuation, which is characterized by the parameter η. In order to determine the attenuation factor, which is the only free fitting parameter, we depict the numerically computed results with various η for $\Omega = \pm 30$ MHz in Figs. 4(b)–4(g). The phase difference appears when η is around 0.1 to 1, and we conclude the optimal fitting parameter is $\eta = 0.5$. We also need to point out the unexpected asymmetry between the amplitudes of positive and negative detunings in Fig. 3. The asymmetry can be attributed to the atom-atom interaction in the BEC [19], which is neglected in the current model.

The superradiant and subradiant TDSs are not eigenstates of the atoms. Nevertheless, in the numerical simulation it is reasonable to make the approximation that the TDSs decay exponentially with two different cooperative decay rates, Γ_{super} for the two superradiant TDSs and Γ_{sub} for subradiant TDSs [18,20,21,29]. The state of the atoms is written as $|\psi(t)\rangle \approx [1 + \sum_j \alpha_j(t) a_j^\dagger + \beta_j(t) b_j^\dagger]|G\rangle$, where $\alpha_j, \beta_j \ll 1$ in the weak-excitation approximation and $|G\rangle = |g_1 g_2 \cdots g_N\rangle$. The equations of motion are obtained as

$$\begin{aligned} \dot{\alpha}_l &= -i\Omega(\beta_l + \beta_{l+1}) - \Gamma_l \alpha_l + \tilde{A}_l \theta(t), \\ \dot{\beta}_l &= -i\Omega(\alpha_l + \alpha_{l-1}) - i\Delta\beta_l, \end{aligned} \tag{3}$$

where $\Gamma_l = \Gamma_{\text{super}}$ for $l = 0, -1$ and $\Gamma_l = \Gamma_{\text{sub}}$ otherwise, $\tilde{A}_l \equiv \tilde{A}[\boldsymbol{k}_f + l(\boldsymbol{k}_1 - \boldsymbol{k}_2)]$, $\tau = 4$ ns is the pulse width, and $\theta(t) = 1$ when $-\tau < t < 0$ and $\theta(t) = 0$ otherwise.

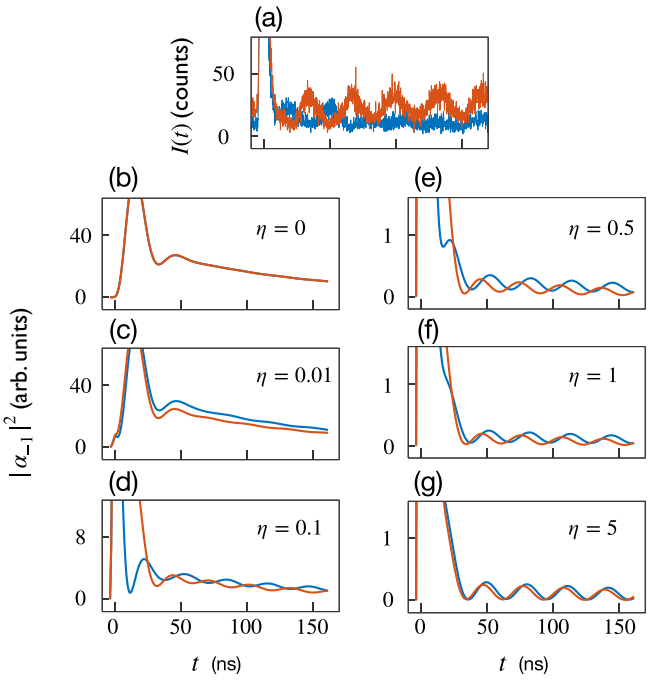

FIG. 4. The attenuation factor η and the phase difference. The coupling laser is detuned from the $|e\rangle$ to $|m\rangle$ transition by −30 MHz [blue (dark gray)] and 30 MHz [red (light gray)]. (a) Experimentally measured photon counts. (b)–(g) Numerically simulated $|\alpha_{-1}|^2$ with $\eta = 0, 0.01, 0.1, 0.5, 1$, and 5. The phase difference between the time-resolved signals for opposite coupling field detunings appears when η is between 0.1 and 1. $\Gamma_{\text{sub}} = 0$. Other parameters are the same as in Fig. 3.

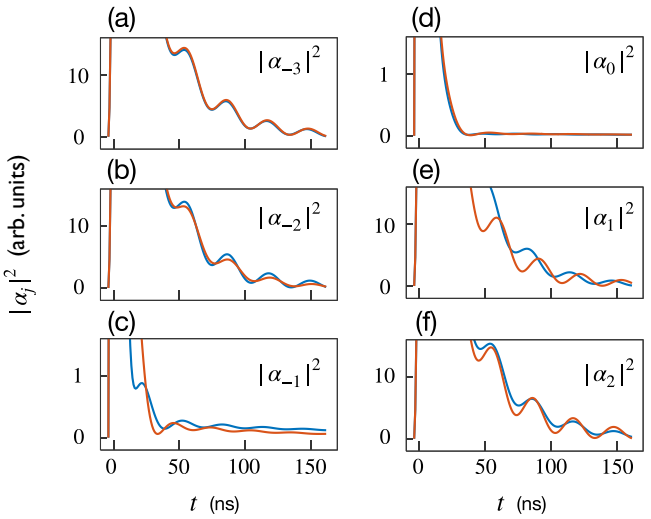

FIG. 5. Numerically simulated $|\alpha_j|^2$. The coupling laser is detuned from the $|e\rangle$ to $|m\rangle$ transition by -30 MHz [blue (dark gray)] and 30 MHz [red (light gray)], $\eta = 0.5$, and $\Gamma_{\text{sub}} = 0.5\gamma$. Other parameters are the same as in Fig. 3.

The oscillation amplitude of the coherent band dynamics strongly depends on the decay rate Γ_{sub} of the subradiant TDSs [18,20,21]. As shown in the experimental data in Fig. 3, the band oscillation continues for a time much longer than $1/\gamma$, which is a signature of subradiance, i.e., $\Gamma_{\text{sub}} < \gamma$ [13,29–36]. Moreover, the oscillation strength depends on the value of Γ_{sub}. In the numerical simulation we vary $\Gamma_{\text{sub}} = 0$, γ, and 2γ. Although the exponential decay envelope is almost the same, the oscillation is smoothed out for $\Gamma_{\text{sub}} \gtrapprox \gamma$, which is more evidence of the subradiant nature of the phase-mismatched TDS.

We also plot the dynamics of $|\alpha_j|^2$ $(j = -3, \ldots, 2)$ for comparison in Fig. 5. The result indicates that the subradiant TDSs have a larger probability than the superradiant ones during the oscillation, owing to their smaller decay rate. It is used to validate that we observe the dynamics of one-dimensional lattices rather than only a few sites. Experimentally, the probability of the subradiant TDSs $|\alpha_j|^2$ $(j \neq 0, -1)$ cannot be obtained by measuring the emission within a certain angle since they do not emit directionally.

IV. CONCLUSION

In this paper, we observed the temporal dynamics of the SL formed by collectively excited states with different phase correlations. The superradiant emission from a superradiant TDS in the SL was measured with subnanosecond resolution. The emission features a fast superradiant emission and a subsequent long-time oscillation. In the backward direction, the early superradiant emission comes from the superradiant TDS initially prepared by the attenuated excitation field, and the oscillation results from the band structure of the SL. The long oscillation time and strong oscillation strength are signatures of the subradiant TDSs in the SL. Our results provide a platform for simulating non-Hermitian lattices with site-dependent decay rates [37–39] and exotic Bloch bands based on atomic cooperativity.

ACKNOWLEDGMENTS

This research is supported by the National Key Research and Development Program of China (Grants No. 2016YFA0301602, No. 2018YFA0307600, No. 2018YFA0307200, and No. 2019YFA0308100) and the National Natural Science Foundation of China (Grants No. 12034011, No. 12004229, No. 11704234, No. 11804203, No. 11974224, No. 12022406, and No. 11874322). S.-Y.Z. was supported by Zhejiang Province Key Research and Development Program (Grant No. 2020C01019).

[1] R. H. Dicke, Coherence in spontaneous radiation processes, Phys. Rev. **93**, 99 (1954).
[2] M. Gross and S. Haroche, Superradiance: An essay on the theory of collective spontaneous emission, Phys. Rep. **93**, 301 (1982).
[3] N. Skribanowitz, I. P. Herman, J. C. MacGillivray, and M. S. Feld, Observation of Dicke Superradiance in Optically Pumped HF Gas, Phys. Rev. Lett. **30**, 309 (1973).
[4] M. Gross, C. Fabre, P. Pillet, and S. Haroche, Observation of Near-Infrared Dicke Superradiance on Cascading Transitions in Atomic Sodium, Phys. Rev. Lett. **36**, 1035 (1976).
[5] M. O. Scully, E. S. Fry, C. H. R. Ooi, and K. Wódkiewicz, Directed Spontaneous Emission from an Extended Ensemble of *N* Atoms: Timing Is Everything, Phys. Rev. Lett. **96**, 010501 (2006).
[6] M. O. Scully and A. A. Svdzinsky, The super of superradiance, Science **325**, 1510 (2009).
[7] T. Bienaimé, R. Bachelard, N. Piovella, and R. Kaiser, Cooperativity in light scattering by cold atoms, Fortschr. Phys. **61**, 377 (2013).
[8] R. A. de Oliveira, M. S. Mendes, W. S. Martins, P. L. Saldanha, J. W. R. Tabosa, and D. Felinto, Single-photon superradiance in cold atoms, Phys. Rev. A **90**, 023848 (2014).
[9] L. Ortiz-Gutiérrez, L. F. Muñoz-Martínez, D. F. Barros, J. E. O. Morales, R. S. N. Moreira, N. D. Alves, A. F. G. Tieco, P. L. Saldanha, and D. Felinto, Experimental Fock-State Superradiance, Phys. Rev. Lett. **120**, 083603 (2018).
[10] P. Tighineanu, R. S. Daveau, T. B. Lehmann, H. E. Beere, D. A. Ritchie, P. Lodahl, and S. Stobbe, Single-Photon Superradiance from a Quantum Dot, Phys. Rev. Lett. **116**, 163604 (2016).
[11] L.-M. Duan, M. D. Lukin, J. I. Cirac, and P. Zoller, Long-distance quantum communication with atomic ensembles and linear optics, Nature (London) **414**, 413 (2001).
[12] S. L. Bromley, B. Zhu, M. Bishof, X. Zhang, T. Bothwell, J. Schachenmayer, T. L. Nicholson, R. Kaiser, S. F. Yelin, M. D. Lukin, A. M. Rey, and J. Ye, Collective atomic scattering and motional effects in a dense coherent medium, Nat. Commun. **7**, 11039 (2016).
[13] W. Guerin, M. O. Araújo, and R. Kaiser, Subradiance in a Large Cloud of Cold Atoms, Phys. Rev. Lett. **116**, 083601 (2016).

[14] M. O. Araújo, I. Krešić, R. Kaiser, and W. Guerin, Superradiance in a Large and Dilute Cloud of Cold Atoms in the Linear-Optics Regime, Phys. Rev. Lett. **117**, 073002 (2016).

[15] P. Weiss, A. Cipris, M. O. Araújo, R. Kaiser, and W. Guerin, Robustness of Dicke subradiance against thermal decoherence, Phys. Rev. A **100**, 033833 (2019).

[16] D. Das, B. Lemberger, and D. D. Yavuz, Subradiance and superradiance-to-subradiance transition in dilute atomic clouds, Phys. Rev. A **102**, 043708 (2020).

[17] S. J. Roof, K. J. Kemp, and M. D. Havey, and I. M. Sokolov, Observation of Single-Photon Superradiance and the Cooperative Lamb Shift in an Extended Sample of Cold Atoms, Phys. Rev. Lett. **117**, 073003 (2016)

[18] M. O. Scully, Single Photon Subradiance: Quantum Control of Spontaneous Emission and Ultrafast Readout, Phys. Rev. Lett. **115**, 243602 (2015).

[19] L. Chen, P. Wang, Z. Meng, L. Huang, H. Cai, D.-W. Wang, S.-Y. Zhu, and J. Zhang, Experimental Observation of One-Dimensional Superradiance Lattices in Ultracold Atoms, Phys. Rev. Lett. **120**, 193601 (2018).

[20] Y. He, L. Ji, Y. Wang, L. Qiu, J. Zhao, Y. Ma, X. Huang, and S. Wu, Geometric Control of Collective Spontaneous Emission, Phys. Rev. Lett **125**, 213602 (2020).

[21] Y. He, L. Ji, Y. Wang, L. Qiu, J. Zhao, Y. Ma, X. Huang, S. Wu, and D. E. Chang, Atomic spin-wave control and spin-dependent kicks with shaped subnanosecond pulses, Phys. Rev. Res. **2**, 043418 (2020).

[22] D.-W. Wang and M. O. Scully, Heisenberg Limit Superradiant Superresolving Metrology, Phys. Rev. Lett. **113**, 083601 (2014).

[23] D.-W. Wang, R.-B. Liu, S.-Y. Zhu, and M. O. Scully, Superradiance Lattice, Phys. Rev. Lett. **114**, 043602 (2015).

[24] A. S. Kuraptsev, I. M. Sokolov, and M. D. Havey, Angular distribution of single-photon superradiance in a dilute and cold atomic ensemble, Phys. Rev. A **96**, 023830 (2017).

[25] P. Wang, L. Chen, C. Mi, Z. Meng, L. Huang, S. N. Khan, H. Cai, D.-W. Wang, S.-Y. Zhu, and J. Zhang, Synthesized magnetic field of a sawtooth superradiance lattice in Bose-Einstein condensates, npj Quantum Inf. **6**, 18 (2020).

[26] A. Schilke, C. Zimmermann, P. W. Courteille, and W. Guerin, Photonic Band Gaps in One-Dimensionally Ordered Cold Atomic Vapors, Phys. Rev. Lett. **106**, 223903 (2011).

[27] S. H. Autler and C. H. Townes, Stark effect in rapidly varying fields, Phys. Rev. **100**, 703 (1955).

[28] E. Saglamyurek, T. Hrushevskyi, A. Rastogi, K. Heshami, and L. J. LeBlanc, Coherent storage and manipulation of broadband photons via dynamically controlled Autler Townes splitting, Nat. Photonics **12**, 774 (2018).

[29] A. Asenjo-Garcia, M. Moreno-Cardoner, A. Albrecht, H. J. Kimble, and D. E. Chang, Exponential Improvement in Photon Storage Fidelities Using Subradiance and Selective Radiance in Atomic Arrays, Phys. Rev. X **7**, 031024 (2017).

[30] D. Pavolini, A. Crubellier, P. Pillet, L. Cabaret, and S. Liberman, Experimental Evidence for Subradiance, Phys. Rev. Lett. **54**, 1917 (1985).

[31] R. G. DeVoe and R. G. Brewer, Observation of Superradiant and Subradiant Spontaneous Emission of Two Trapped Ions, Phys. Rev. Lett. **76**, 2049 (1996).

[32] M. D. Barnes, P. S. Krstic, P. Kumar, A. Mehta, and J. C. Wells, Far-field modulation of fluorescence decay rates in pairs of oriented semiconducting polymer nanostructures, Phys. Rev. B **71**, 241303(R) (2005).

[33] Y. Takasu, Y. Saito, Y. Takahashi, M. Borkowski, R. Ciuryło, and P. S. Julienne, Controlled Production of Subradiant States of a Diatomic Molecule in an Optical Lattice, Phys. Rev. Lett. **108**, 173002 (2012).

[34] P. Weiss, M. O. Araújo, R. Kaiser, and W. Guerin, Subradiance and radiation trapping in cold atoms, New J. Phys. **20**, 063024 (2018).

[35] V. V. Temnov and U. Woggon, Superradiance and Subradiance in an Inhomogeneously Broadened Ensemble of Two-Level Systems Coupled to a Low-Q Cavity, Phys. Rev. Lett. **95**, 243602 (2005).

[36] T. Bienaimé, N. Piovella, and R. Kaiser, Controlled Dicke Subradiance from a Large Cloud of Two-Level Systems, Phys. Rev. Lett. **108**, 123602 (2012).

[37] S. Lapp, J. Ang'ong'a, F. A. An, and B. Gadway, Engineering tunable local loss in a synthetic lattice of momentum states, New J. Phys. **21**, 045006 (2019).

[38] W. Gou, T. Chen, D. Xie, T. Xiao, T.-S. Deng, B. Gadway, W. Yi, and B. Yan, Tunable Nonreciprocal Quantum Transport through a Dissipative Aharonov-Bohm Ring in Ultracold Atoms, Phys. Rev. Lett. **124**, 050502 (2020)

[39] Y. Li, H. Cai, D.-W. Wang, L. Li, J. Yuan, and W. Li, Many-Body Chiral Edge Currents and Sliding Phases of Atomic Spin Waves in Momentum-Space Lattice, Phys. Rev. Lett. **124**, 140401 (2020).